Physical Modeling of RF Through-the-Wall Mapping using FEM

Rafael Saraiva Campos, Lisandro Lovisolo and Marcello L. R. de Campos

***Abstract*— Radiofrequency (RF) Through-the-Wall Mapping (TWM) employs techniques originally applied in Computerized Tomographic Imaging to map obstacles behind walls. Therefore, it can provide valuable information in military operations in urban scenarios, as well as in rescuing efforts in damaged buildings. This work proposes applying Finite Element Method (FEM) to simulate a parallel-beam geometry RF TWM setup. The use of FEM simulations allows faster evaluation of different reconstruction algorithms for several geometries and materials. Furthermore, due to time and budgetary constraints, sometimes field measurements campaigns cannot be carried out. A test floor blueprint was defined, and Filtered Backprojection Reconstruction was applied to recover the floor map. The achieved results were compared to results obtained through field measurements and available in the literature. To the best of our knowledge, this is the first use of FEM simulations in a TWM problem.**

***Keywords*— Radiofrequency, Through-the-Wall Mapping, Filtered Backprojection Reconstruction, Finite Element Method.**

I. Introduction

RF Through-the-Wall Mapping (TWM) aims at identifying the location of static obstacles without sensing them directly. Therefore, it provides a non-invasive way to build a floor map using RF electromagnetic waves [1]. The capability to obtain an estimate of the floor blueprint, before entering the room, can provide valuable information in military operations, such as urban combat and hostage situations [2], as in such cases direct obstacle mapping with specialized sensors (laser, ultrasound, infrared, etc.) on-board a mobile robot is not an option, due to the presence of hostile forces and the need for a stealth approach. RF TWM can also be used in situations when the area to be mapped is not accessible due to physical constraints, such as in damaged buildings. Consequently, RF TWM can improve tactical situation awareness in critical conditions [3].

This work proposes the use of Finite Element Method (FEM) to simulate a parallel-beam geometry RF TWM setup. A geometry representing a floor blueprint with concrete walls and a central pillar is defined, and the Radon projections are acquired through propagation simulations at 1 GHz. Following, Filtered Backprojection Reconstruction is used to recover the floor map. The use of FEM simulations allows faster evaluation of different reconstruction algorithms for several geometries and materials. Apart from that, sometimes, due to time and budgetary constraints, field measurements cannot be collected. To the best of our knowledge, this is the first use of FEM simulations in a TWM problem.

Rafael Saraiva Campos (PEE/COPPE/UFRJ, CEFET/RJ), Lisandro Lovisolo (PROSAICO/PEL/DETEL/UERJ), Marcello L. R. de Campos (PEE/COPPE/UFRJ). E-mails: rafael.campos@cefet-rj.br, lisandro@uerj.br, campos@smt.ufrj.br.

The remainder of this paper is organized as follows: Section II introduces the key concepts related to image reconstruction from parallel-beam projections; Section III discusses some RF electromagnetic wave propagation issues related to TWM; Section IV presents the basics of FEM; Section V details the implementation of the proposed parallel-beam geometry RF TWM setup in an FEM software, and presents the simulation results. Finally, Section VI brings a brief conclusion.

II. Image Reconstruction from Parallel-Beam Projections

Parallel-beam geometry and its associated imaging reconstruction techniques were the basis for the first generation of X-ray Computerized Tomographic Imaging (CTI) [4]. The Radon transform and the Fourier Central Slice theorem provide the mathematical foundations for those reconstruction techniques.

A. Radon Transform

Consider line r in Fig. 1a, defined by $y = (\tan\gamma)\,x + b$, where $(0, b)$ are the coordinates of point B, which is the intersection of r and the y axis. From triangle OCA, one gets that $\gamma = \theta_k + \pi/2$, so $\tan\gamma = -1/\tan\theta_k$. From triangle OCB, one verifies that $b = \rho_j / \sin\theta_k$. Therefore, $y = -x/\tan\theta_k + \rho_j/\sin\theta_k$, which can be rewritten as $x\cos\theta_k + y\sin\theta_k = \rho_j$. A parallel-beam can be defined by a set of such lines (rays), varying the value of ρ for a fixed θ, as depicted in Fig. 1b.

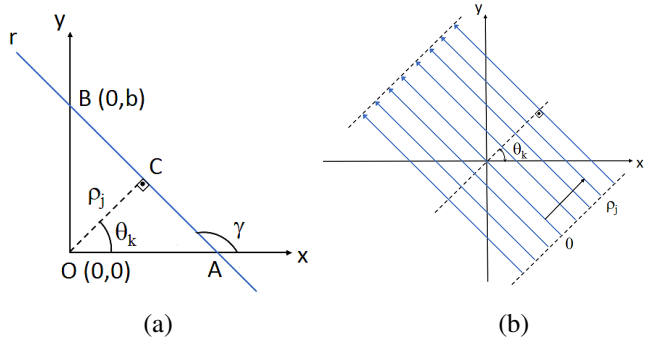

Fig. 1. (a) Defining the line equation using polar parameters; (b) Parallel-ray beam for $\theta = \theta_k$.

Assume that the rays in the parallel beam represent the propagation path of electromagnetic energy traveling between a transmitter (TX)/receiver (RX) pair, moving along L-meter

parallel paths, as shown in Fig. 1b. If the energy passes through an object positioned along the propagation path, part of the energy will be absorbed by the object. Then, a projection will be obtained at the receiver end, where the absorption characteristics of that object will be imprinted. Assuming that the output energy is known, the absorption through the object along a trajectory specified by θ_k and ρ_j can be inferred from the received energy. This absorption is given by the line integral

$$g(\rho_j, \theta_k) = \int_{-\infty}^{+\infty} \int_{-\infty}^{+\infty} f(x, y)\delta(x\cos\theta_k + y\sin\theta_k - \rho_j)dxdy \quad (1)$$

where $f(x, y)$ is the absorption rate of the object cross-section at coordinates (x, y). The impulse function indicates that the integration is carried out along the line $x\cos\theta_k + y\sin\theta_k = \rho_j$.

Eq. (1) is the Radon transform of function f in the xy-plane along the direction defined by θ_k and ρ_j [5]. Projection $g(\rho, \theta_k)$ is obtained applying Eq. (1) for all $\rho \in [-L/2; L/2]$. After calculating the projections for all $\theta \in [0; \pi)$, one obtains the *sinogram* of the original image.

B. Fourier Central Slice Theorem

The Fourier Central Slice theorem states that the 1-D Fourier Transform (FT) of a Radon projection of an image taken at angle θ_k is equal to the slice of the 2-D FT of that image, taken at that same angle. The 1-D FT of a Radon projection at angle θ_k with respect to spatial variable ρ is given by

$$G(\mathrm{f}, \theta_k) = \int_{-\infty}^{+\infty} g(\rho, \theta_k)e^{-j2\pi \mathrm{f}\rho}d\rho \quad (2)$$

where f is the spatial frequency. Replacing $g(\rho, \theta_k)$ in Eq. (2) by the expression provided by Eq. (1), and solving the innermost integral using the impulse sampling property, one gets

$$G(\mathrm{f}, \theta_k) = \int_{-\infty}^{+\infty} \int_{-\infty}^{+\infty} f(x, y)e^{-j2\pi(\mu x + \nu y)}dxdy \quad (3)$$

where $\mu = \mathrm{f}\cos\theta_k$ and $\nu = \mathrm{f}\sin\theta_k$, are the frequency variables. The right side of Eq. (3) is a central slice of the 2-D FT of $f(x, y)$, taken at angle θ_k.

C. Filtered Backprojection Reconstruction

Reconstruction is the recovery of the original image from its sinogram. It might be carried out through backprojections, where each Radon projection is smeared over the image along the parallel beam direction. This section introduces the principles of Filtered Backprojection Reconstruction (FBR), which is the most widely used technique in CTI [4].

Function $f(x, y)$ expresses the absorption rate of the object cross-section at planar coordinates (x, y). The 2-D FT of $f(x, y)$ is given by $F(\mu, \nu)$, from which follows that $f(x, y)$ is the inverse 2-D FT of $F(\mu, \nu)$. In polar coordinates, it is given by:

$$f(x, y) = \int_0^{2\pi} \int_0^{+\infty} F(\mathrm{f}\cos\theta, \mathrm{f}\sin\theta)e^{j2\pi \mathrm{f}(x\cos\theta + y\sin\theta)}\ \mathrm{f}\ d\mathrm{f}\ d\theta \quad (4)$$

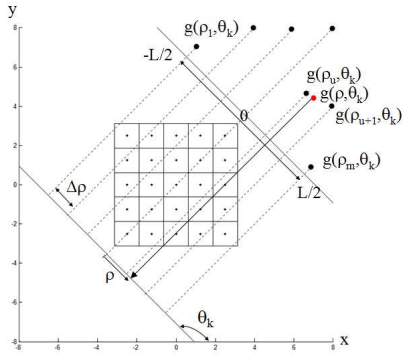

Fig. 2. The Radon projection at angle θ_k is sampled at m points (dark dots in the image); as a result, the value $g(\rho, \theta_k)$ to be backprojected over the pixels (of the reconstructed image) along the line defined by (ρ, θ_k) must be obtained by interpolation.

From Eq. (3)), one gets that $F(\mathrm{f}\cos\theta, \mathrm{f}\sin\theta) = G(\mathrm{f}, \theta)$, where $G(\mathrm{f}, \theta)$ is the FT of the Radon projection $g(\rho, \theta)$. Replacing that value in Eq. (4) and using some trigonometry yields:

$$f(x, y) = \int_0^{\pi} \left(\int_{-\infty}^{+\infty} |\mathrm{f}|\ G(\mathrm{f}, \theta)e^{j2\pi \mathrm{f}\rho}d\mathrm{f} \right) d\theta \quad (5)$$

where the inner integral provides $\mathcal{F}^{-1}\{|\mathrm{f}|\, G(\mathrm{f}, \theta)\}$, i.e, the inverse 1-D FT of $G(\mathrm{f}, \theta)$ multiplied by a ramp filter. Eq. (5) states that the original image $f(x, y)$ can be reconstructed by backprojecting $\mathcal{F}^{-1}\{|\mathrm{f}|\, G(\mathrm{f}, \theta)\}$. In the practical discrete case, Eq. (5) becomes an approximation given by:

$$\hat{f}(x, y) = \Delta\theta \sum_{\theta=0}^{n} \mathcal{F}^{-1}\{|\mathrm{f}|\, G(\mathrm{f}, \theta)\} \quad (6)$$

where $\mathcal{F}^{-1}$ indicates the inverse 1-D Discrete FT (DFT) operator, and a 1-D interpolation is required in the backprojection, as shown in Fig. 2. The ramp filter reinforces the high frequency components, compensating for the sparser sampling at high frequencies. This reduces blurring in the reconstructed image. To prevent ringing, the ramp filter transfer function is multiplied by a Hamming window [4].

III. RF Electromagnetic Wave Propagation Issues

A. Multipath Propagation and Ray Bending

The parallel-beam geometry assumes straight single path propagation, i.e., it disregards multipath arising from reflections at interfaces and diffraction around corners, as well as ray deviation due to refraction. While this assumption holds true for X-Ray tomography, due to the very small wavelength, the same does not apply to RF TWM. If the transmitted energy is reaching the receiver through different paths, it is not possible to accurately estimate the loss through each section of the object being mapped (as, besides constructive and destructive interference of the multiple received components, they do not necessarily pass through the object), causing reconstruction errors.

B. Operational Frequency Selection

The main issues concerning the operational frequency selection for RF TWM are specific attenuation, diffraction, and interference from external sources. The first two – specific attenuation (dB/m) and diffraction – are interchangeable: the higher the frequency, the higher the specific attenuation, but the lower the energy of the diffracted components (which reduces reconstruction error). In the opposite direction, lower frequencies, though experiencing less through-the-wall attenuation, are more prone to diffraction effects. A trade-off between those two issues must be set for a proper operational frequency to be selected.

Specific attenuation, together with transmitter effective isotropic radiated power (EIRP) and receiver sensitivity, limits the maximum admissible path loss, restricting the largest floor that can be mapped. For example, propagation losses through concrete at 3 GHz are so high (66 dB/m [6]) that using RF TWM becomes unfeasible with low power transmitters. At 1 GHz, the wavelength is long enough for diffraction to be relevant, but through-the-wall losses are much lower. Frequencies around 2 GHz are to be avoided, due to possible external interference by WiFi networks.

IV. Finite Element Method

The Finite Element Method (FEM) is a numerical tool suitable for the solution of general *field problems*, like elasticity, fluid flow, heat transfer, and electromagnetic wave propagation. Those problems have *field variables* that must be calculated subjected to specific *boundary conditions*. The field variables are governed by differential equations. The boundary conditions are the specified values of the field variables on the boundaries of the field [7].

A key concept in FEM is the discretization or *meshing*, which is the process of dividing the model geometry into smaller units called *finite elements*. Those units are interconnected at points (1D geometry), boundary lines (2D geometry) or boundary surfaces (3D geometry), common to two or more elements. The *nodal points* are the vertexes of the finite elements. The field variables must be explicitly calculated at the nodal points, using the problem governing differential equations. The values of the field variables are estimated at non-nodal points using interpolation functions, also referred to as *shape functions*. The number of *degrees of freedom* is equal to the number of finite elements, multiplied by the number of nodal points per element and by the number of values of the field variables that must be calculated at each node [8].

V. TWM FEM Simulation

Simulations of indoor RF propagation typically rely on empirical path loss equations, such as $L_d = \beta + \gamma \log\left(\frac{d}{d_0}\right)$, where β is the propagation loss (dB) at a distance d_0 meters from the transmitter and γ is the path loss slope (dB/m). Calibration campaigns are required to fine tune such models before they can be applied to a specific environment. These propagation models assume single-path straight line propagation, disregarding multipath, refraction and diffraction. In an attempt take the effect of multipath into consideration, Rician or Rayleigh distributions are commonly used to provide an additional random path loss component [1], [9]. However, this empirical formulation is too simplistic, so the simulation output when using these models is unrealistically (and deceivingly) accurate, as the dashed line in Fig 6 shows.

Compared to the aforementioned method, an FEM RF propagation simulation is capable of providing much more realistic results, as it models the electromagnetic wave interaction with different physical media with much higher detail and fidelity [10], [11].

This section describes the FEM simulation of the parallel-beam geometry TWM setup. The simulation was carried out in COMSOL Multiphysics®, a commercial package which can be applied to electromagnetic wave propagation problems.

A. Governing Equations and Boundary Conditions

In the TWM FEM simulation, the Helmholtz vector equation for harmonic electric fields

$$\nabla \times \nabla \times \vec{E}\ (\vec{r}, t) + \gamma^2 \vec{E}\ (\vec{r}, t) = 0 \tag{7}$$

is solved at each nodal point, where $\vec{E}\ (\vec{r}, t)$ is the electric field vector in volts per meter (V/m) at instant t at location $\vec{r}$ and γ is the complex propagation constant, given by $\gamma = \sqrt{j\omega\mu\,(\sigma + j\omega\epsilon)}$, where ω is the harmonic field angular frequency (rad/s), σ is the material electrical conductivity in siemens per meter (S/m), μ is the material magnetic permeability in henries per meter (H/m) and ϵ is the material electric permittivity in Farads per meter (F/m). The field variables solutions are subjected to the boundary conditions for the electric and magnetic fields:

$$\left(\vec{E}_1 - \vec{E}_2\right) \times \vec{n} = 0; \quad \left(\vec{D}_1 - \vec{D}_2\right) \cdot \vec{n} = \rho_s \tag{8}$$

$$\left(\vec{H}_1 - \vec{H}_2\right) \times \vec{n} = \vec{K}; \quad \left(\vec{B}_1 - \vec{B}_2\right) \cdot \vec{n} = 0 \tag{9}$$

where $\vec{n}$ is a unitary vector normal to the boundary between media 1 and 2, $\vec{K}$ is the surface current density in amperes per meter (A/m), ρ_s is the surface charge density in coulombs per square meter (C/m^2), $\vec{D} = \epsilon\vec{E}$ is the electric flux density vector (C) and $\vec{B} = \mu\vec{H}$ is the magnetic flux density vector in weber (Wb). There are only dielectric materials in the model geometry, so $\rho_s = 0$ at all boundaries and $\vec{K}$ is different from zero only at the TX monopole (the field source, described in Section V-D).

B. Model Geometry, Materials and Meshing

The main obstacles present in a floor – walls and doors – have a constant horizontal cross section. Considering this symmetry, a planar 2D Model can be used in the FEM simulation. In that case, using a 2D model instead of a 3D one allows creating a denser mesh, with smaller finite elements, which improves the simulation accuracy. The maximum size of the triangular finite elements was set to $\lambda/5$ [12], where $\lambda = 30$ cm is the wavelength at 1 GHz.

The 2D model defined in the FEM software consists of an 8×8 m^2 floor, with a 1.6×1.6 m^2 pillar placed at its center. The 0.5 m-thick outer walls and the central pillar are made of concrete. The floor is immersed in a dry atmosphere and surrounded by a perfect matching layer (PML), which is a circular boundary placed around the model's geometry

to prevent reflections at the outermost interface [12]. The PML width is 0.9 m, which corresponds to 3λ. The model geometry is depicted in Fig. 3a. The electromagnetic properties – electrical conductivity (σ), relative electric permittivity (ϵ_r) and relative magnetic permeability (μ_r) – of the materials used in the model are: i) air: $\epsilon_r = \mu_r = 1$ and $\sigma = 0$; ii) concrete (solid, dry): $\epsilon_r = 7$, $\mu_r = 1$ and $\sigma = 0.04733$ S/m [13].

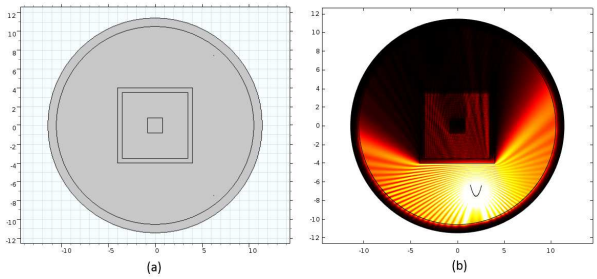

Fig. 3. (a) Floor blueprint, with four walls and a central pillar, surrounded by the PML; (b) Surface map of the vertically polarized electric field norm. Note that the antenna reflector is also visible in the figure.

C. Antenna Design

As a 2D planar model is being used, it is necessary to select an antenna with a constant horizontal cross section, such as a monopole with a cylindrical parabolic reflector [14]. Due to the extremely small skin depth at 1 GHz in metals, the reflector was configured as a perfect electrical conductor surface (no width, zero skin depth). The monopole center was placed at the focal line of the reflector. Fig. 4a shows the antenna horizontal cross section. After testing different configurations, the selected antenna parameters were: $r = 1$ cm (monopole radius), $p = \lambda/4 = 7.5$ cm (focal distance), $D = 1.2$ m (reflector aperture) and $L = (0.5D)^2/4p = 1.2$ m.

The horizontal radiation pattern of the antenna at 1 GHz shown in Fig. 4b was obtained through FEM simulations, placing the receiver probe in the far field region (i.e., farther than the Fraunhofer distance [15]). At the selected central frequency, the designed antenna has a maximum gain of 14 dBi, 20 degrees half-power beamwidth, and a 30 dB front-to-back ratio.

A high antenna gain is required to minimize the effects of multipath reception. However, for a fixed operational frequency, there is a trade-off between the antenna gain and antenna dimensions: as the sinogram acquisition process requires moving the TX/RX pair through several locations, the antenna cannot be too large. The dimensions of the designed antenna allow it to be placed on the roof of a car, or on-board a mobile robot.

D. Field Source and Receiver Probe

To excite the RF model, a surface current density $\vec{K} = 1.6 \sin(2\pi f t)\, \hat{a}_z$ (A/m) is set over the TX monopole boundary, with $f = 1$ GHz. This generates a vertically polarized (perpendicular to the model plane) electromagnetic wave. A boundary probe is defined on the RX monopole, integrating the received

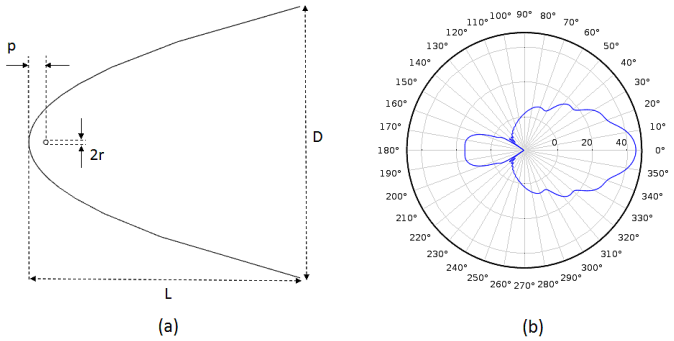

Fig. 4. (a) Cross-section of the monopole and the cylindrical parabolic reflector; (b) Horizontal radiation pattern of the antenna.

electric field norm over the monopole's boundary. Identical antennas are used in both transmission and reception.

E. Sinogram Acquisition

To acquire the sinogram using a parallel-beam geometry, Radon projections were obtained at 20 angles uniformly spaced in [0,π), i.e., $\Delta\theta = 9$ degrees. At each projection, 140 samples were collected, with a linear spacing $\Delta\rho = 9$ cm. So, the sinogram has 2800 samples. For each collected sample, the electromagnetic propagation over the entire test area must be calculated. In this simulation, it was assumed that the receiver (not represented in the model) has a sensitivity capable of detecting the received signal at all sample locations, i.e., there is no "clipping" of the Radon projection (which would occur if the received signal level were below the receiver sensitivity).

F. Reconstruction Results

Fig. 5 summarizes the reconstruction process. Fig. 5a shows the floor blueprint. Fig 5b presents the sinogram that would be obtained using the parallel-beam geometry if there was no refraction, diffraction or reflections (which would be an ideal condition, though unrealistic and unfeasible). Fig 5c depicts the sinogram provided by the FEM simulation, to which a 2D median filter is applied, yielding the sinogram shown in Fig 5d. This low pass filter is used to smooth fluctuations in the received signal due to multipath propagation. The effect of this filtering can be better evaluated in Fig. 6, which shows the Radon projections obtained at $\theta = 0$ degrees before (a) and after (b) applying the median filter. Note that the attenuation spikes at $\rho = \pm 2$ m are almost completely filtered out. All sinograms and individual Radon projections are expressed in the logarithmic scale (dB).

Fig. 6e shows the image obtained by FBR. Finally, Fig. 6f brings the recovered floor blueprint, after applying a threshold filter and then a 2D median filter. The threshold filter converts Fig. 6e to a binary image, setting any pixel luminance below $(M - 8)$ dB to 0, and any intensity above that level to 1, where M is the maximum pixel luminance intensity of the image shown in Fig. 6e.

The final result illustrated in Fig. 6f allows clear identification of the outer walls and the central obstacle. This result is comparable to the reconstructed images (using Direct Fourier Reconstruction [5]) obtained through field measurements in [1].

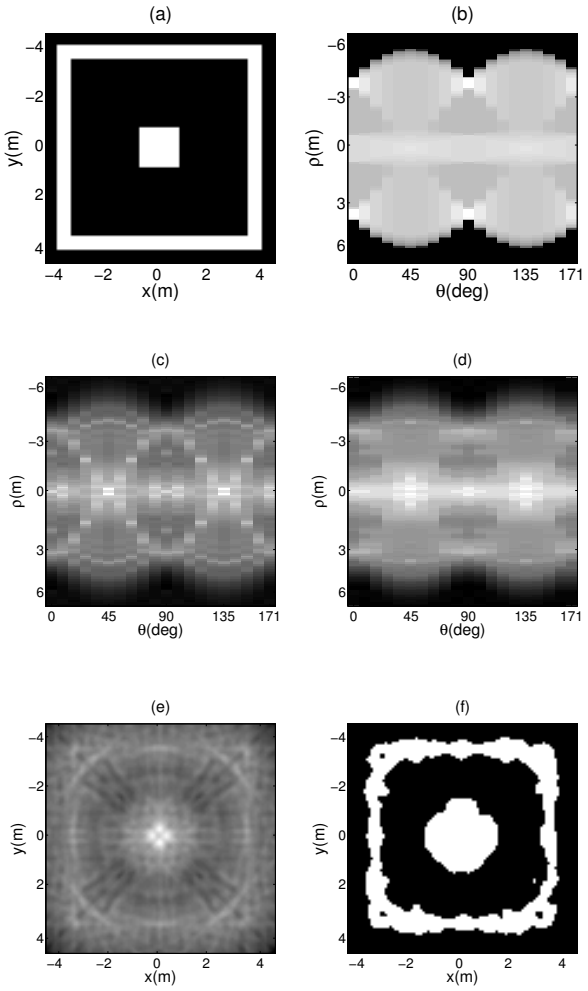

Fig. 5. (a) Floor blueprint; (b) Sinogram (in log. scale) assuming straight (no refraction) single-path (nor reflection neither diffraction) propagation; (c) Sinogram (in log. scale) obtained from the FEM simulation; (d) Sinogram after applying a 3×3 median filter to (c); (e) FBR recovered image; (f) Recovered floor blueprint after applying a threshold filter to (e), followed by a 5×5 median filter.

VI. Conclusions

This work proposed applying FEM to simulate a parallel-beam geometry RF TWM setup. The use of FEM simulations allows faster evaluation of different reconstruction algorithms for several geometries and materials. Furthermore, due to time and/or budgetary constraints, sometimes field measurements campaigns cannot be carried out.

A test floor blueprint was defined and FBR was applied to recover the floor map. The achieved results were validated and compared to results obtained with field measurements and available in the literature. To the best of our knowledge, this is the first use of FEM simulations in a TWM problem.

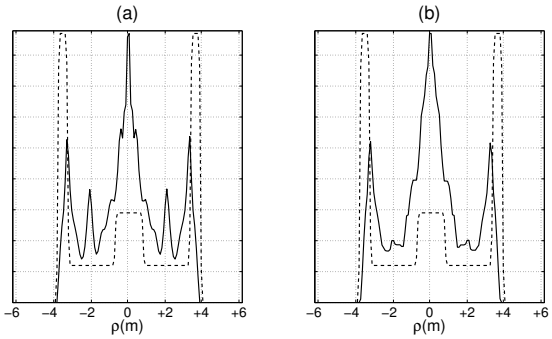

Fig. 6. (a) Before 2D median filtering; (b) After 2D median filtering. The dashed line in both figures represent the Radon projection that would be obtained without ray bending (no refraction) and with single path (no reflection nor diffraction) propagation, which would be an ideal condition, though unrealistic and unfeasible in RF TWM.

As future developments, the authors plan to evaluate other reconstruction algorithms, such as Algebraic Reconstruction, and configure more complex model geometries, attempting to pinpoint the location of doors, gateways and windows on interior walls, as well as simulating walls with different materials (brick, reinforced concrete, wood, etc.).

References

[1] Y. Mostofi, "Compressive Cooperative Sensing and Mapping in Mobile Networks", *IEEE Transactions on Mobile Computing*, v.10, n.12, pp 1769–1784, Dec 2011.

[2] M. Bjorkbom et al, "Localization Services for Online Common Operational Picture and Situation Awareness", *IEEE Access*, v. 1, pp. 742–757, October 2013.

[3] M. R. Endsley, "Towards a Theory of Situation Awareness in Dynamic Systems", *Human Factors: The Journal of the Human Factors and Ergonomics Society*, v.1, n. 37, pp. 32–64, March 1995.

[4] R. C. Gonzalez and R. E. Woods, "Digital Image Processing", Pearson Prentice Hall, 3rd ed., 2008.

[5] A. C. Kak and M. Slaney, "Principles of Computerized Tomographic Imaging", IEEE Press, 1st ed., 1988.

[6] C. D. Taylor et al, "Measurement of RF Propagation into Concrete Structures over the Frequency Range 100 MHZ to 3 GHz", *Wireless Personal Communications*, v. 377, pp. 131–144, 1997.

[7] E. Barkanov, "Introduction to the Finite Element Method", Institute of Materials and Structures - Faculty of Civil Engineering - Riga Technical University, 2001.

[8] A. Tura, "A Review of Finite Element Analysis Method", Computer Aided Design Course (Lecture Notes), Faculty of Engineering- University of Victoria, 2014.

[9] D. Puccinelli and M. Haenggi, "Multipath Fading in Wireless Sensor Networks: Measurements and Interpretation", *Proceedings of the 2006 International Conference on Wireless Communications and Mobile Computing*, pp. 1039–1044, Vancouver, Canada, 2006.

[10] T. Hult and A. Mohammed, "Multipath Propagation Assessment for a 2.4 GHz Short-Range Wireless Communication System", *IEEE First European Conference on Antennas and Propagation*, pp. 1–5, Nice, France, Nov 2006.

[11] H. T. Anastassiu et al, "A Computational Model for Path Loss in Wireless Sensor Networks in Orchard Environments", *Sensors*, n. 14, pp. 5118–5135, 2014.

[12] COMSOL, "RF Module User's Guide, version 4.3", Tech. Manual, p. 31–37, 2012.

[13] ITU, "ITU-R P.1238: Prop. Data and Prediction Models for the Planning of Indoor Radiocom. Systems and Radio LANs in the Freq. Range 900 Mhz to 100 GHz"', Tech. Recommendation, 1997.

[14] H. M. Zali et al, "Design of a Cylindrical Parabolic Reflector on Monopole Plasma Antenna", *Proceedings of IEEE International RF and Microwave Conference*, pp 344–348, Penang, Malaysia, Dec 2013.

[15] W. L. Stutzman and G. A. Thiele, "Antenna Theory and Design", Wiley, 3rd ed., 2013.